Aalborg Universitet

Optimized Design of Embedded Air Coil for Small Satellites with Various Dimensions

Khan, Shoaib Ahmed ; Ali, Anwar; Yang, Shiyou; Tong , Jijun ; Guerrero, Josep M.

Analysis and Design of Embedded Printed Air-Coil for Various Dimensions Small Satellites

Shoaib Ahmed Khan[1], Yang Shiyou[3],
College of Electrical Engineering, Zhejiang University, Hangzhou 310027, China

Anwar Ali[2], Jijun Tong[4]
School of Information Science and Technology, Zhejiang Sci-Tech University, Hangzhou 310018, China

Josep M. Guerrero[5]
Institute of Energy Technology, Aalborg University, Aalborg 9220, Denmark

Abstract- Active attitude control systems using a novel six layers electromagnetic embedded printed Air-Coils for small satellites with various dimensions are presented in this paper. The proposed designs are optimized in terms of available area, generated torque, power dissipation and generated magnetic dipole moment. The designed printed Air-Coils are the best choice for small satellites attitude stabilization in terms of their modularity, reconfigurability, lower cost, lesser space occupation and low mass. The printed Air-Coil is designed and analyzed for three small satellites with dimensions 10 cm^3, 13cm^3 and 16cm^3. The design is implemented with Commercial off the shelf (COTS) microdevices which are inexpensive, reliable and easily accessible. The printed Air-Coil is integrated in internal layers of printed circuit board (PCB) which does not require additional space on the spacecraft. The proposed Air-Coil with additional configurability features (2×3, 3×2 hybrid) provide more flexibility to the design aspects by changing the arrangement through the onboard processor according to mission requirements. Electrothermal analysis of the Air-Coil module is done to keep the thermals in check and validate its feasibility. Time varying rotational operation of nanosatellites is performed to test the rotation time for spin stabilized satellites. Significant performance parameters like generated magnetic moment, resultant torque and power dissipation are evaluated and compared with the already commercial state of the art.

I. Introduction

The exploration and exploitation of space has been a very expensive but invaluable endeavor that has given us a

---

[1] PhD Scholar, College of Electrical Engineering, Zhejiang University.
[2] Associate Professor, School of Information Science and Technology, Zhejiang Sci-Tech University.
[3] Professor, College of Electrical Engineering, Zhejiang University.
[4] Professor, School of Information Science and Technology, Zhejiang Sci-Tech University.
[5] Professor, Institute of Energy Technology, Aalborg University.

vast understanding of our planet, distant worlds and wonders of universe. So far, 2062 active artificial satellites orbit the Earth and human beings takes the everyday benefits of space for granted, whether it be for weather forecasting, man-made disasters or navigation & communication [1],[2]. Modern nanosatellites in many cases now compete and in some aspects transcends the capabilities of conventional large satellites but at a fraction of cost [3]. The revolution in nanoelectronics production techniques developed for the consumer mass market implies that the testing and performance certainty can be achieved at subsystem level instead of using individual components. Thus, commercial off the shelf (COTS) microdevices for the development of small satellites are inexpensive, reliable and easily available [4]–[7]. The small size, mass, cost, low power operation, scalability and modularity features make them a suitable choice for universities and small & medium enterprises (SMEs). Academic institutions are working on various projects of small satellites and therefore provide a testbed to innovation (e.g. Hardware and software) that can be further implemented in large and expensive missions [8]–[14]. Satellites classification on the basis of their design features, weights and sizes is given in [15], [16]

Making the spacecraft smaller poses a great challenge and requires engineering ingenuity to house large number of crucial subsystems such as power management, attitude control, telecommunication and payload etc. [17]. Attitude control system (ACS) is the most critical subsystem of any spacecraft and is used for the orientation and stabilization of directional components for small satellites that needs to be directed and positioned at specific inertial frame of axis e.g. solar panel towards the sun and antennas towards the ground station [18]–[21]. The ACS should let the payload track the specific objects on Earth or maneuver its optical instruments towards astronomical objects. Attitude control system is used for the stabilization and maneuverability while the attitude determination system estimates or senses the attitude of the vehicle e.g. magnetometer, sun tracker and gyroscope [22], [23]. Stabilization and maneuverability of satellites can be categorized into two types, passive stabilization and active stabilization.

Passive stabilization methods depend on gravity gradients, solar radiation pressure, permanent magnets, aerodynamics, and Earth's magnetic field. Gravity gradient passive stabilization utilizes a boom that interacts with the gravitational force to stabilize the vehicle. The boom lets the center of gravity push towards itself due to which torque is created, one face of the satellite moves downwards and boom is aligned in the direction of the Earth. In orbital transfer, the gravity gradient based nanosatellite under a continual thrust show complex dynamic behavior. Magnetorquer is used in conjunction with gravity gradient which provides a control torque that provides stabilization mainly in two axes due to which auxiliary compensators are used. Thus, making the overall system complicated [24].
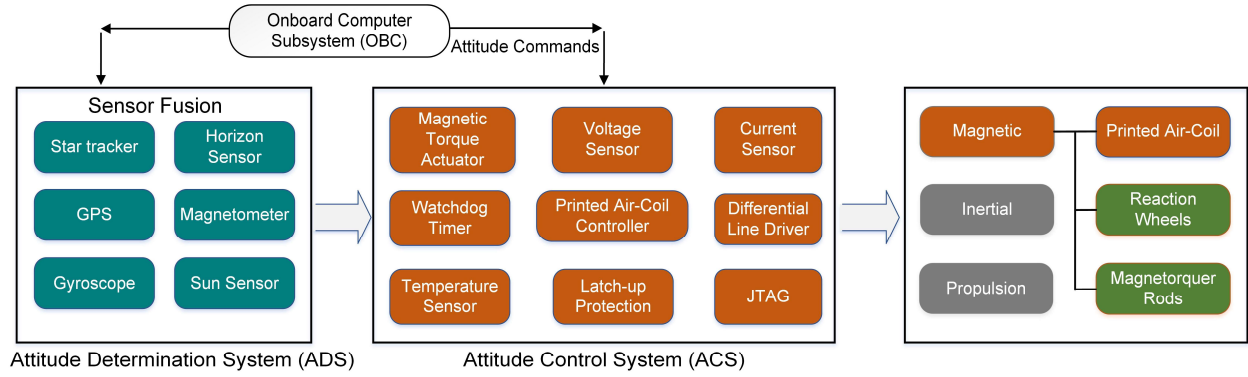
Fig. 1 Block level representation of ADS and ACS communication with onboard computer system (OBC)

Advantages of this design are simplicity, long lifetime, and consumes no power. Recently, permanent magnet based passive attitude stabilization has gained the interest of researchers in the development of small satellites for Low Earth Orbit (LEO) missions [25]–[27]. In this system passive magnets with a set of hysteresis rods are used. The system allows to maneuver and follow the vehicle in Earth's local magnetic field vector. In [28] the authors propose various approaches for enhancement of versatility, efficiency, and robustness of hall type thrusters using permanent magnets over traditional electromagnetic coils. However, design and testing of hall thrusters poses a considerable challenge that requires large and state of the art instruments and data acquisition systems [29], [30]. The techniques required to develop these systems pose considerable number of challenges to effectively utilize magnetic forces, low attitude accuracies and unavailability of forces [31].

For optimal pointing accuracy, active stabilization methods (magnetic rods, reaction wheels and spin control systems) are used for three axis maneuverability of spacecraft [32]–[35]. The motor-driven reaction wheel is one of the most widely used active stabilization component by regulating motor torque for the attitude control owing to its exceptional pointing accuracy [36]. Despite their high pointing accuracies [37], these momentum exchange systems may experience saturation limitations and static friction when they approach zero angular velocity [38]. Hence, reaction wheels require a secondary ACS for momentum unloading and desaturation of the reaction wheels system. So, they need magnetorquers energy efficient, reliable, and effective external torque for momentum desaturation purposes [39]–[42]. Active stabilization systems control precise vehicle orientation to practically any desired degree of accuracy. But these methods are expensive to implement as they require propellant or energy which leads to increase in weight, power and size constraints.

This work proposes solution for light weight, energy efficient active ACS using a novel six-layer printed Air-Coil to optimize the design in terms of available area, generated torque and dipole moment. The principle of operation is
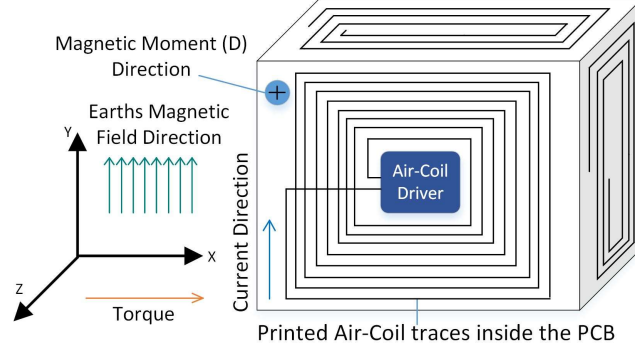
Fig. 2 Earth's magnetic field interaction with printed Air-Coil's magnetic moment

the generation of magnetic field from coil as the current flows through it resulting in the interaction of Earth's magnetic field and required torque is provided according to motor action principle. In [43] the authors discuss significant advantages of reconfigurable design parameters over the already available commercial magnetorquers[44]–[46]. The block diagram of printed Air-Coil unit is depicted in Fig. 1.

This work presents the optimized design for nanosatellites having dimensions of $10\ cm^3$, $13\ cm^3$, and $16\ cm^3$. The optimized reconfigurable printed design and performance parameters are compared with the commercial magnetorquers that require high expenditure. The printed Air-Coil generates heat inside the Air-Coil module. Therefore, thermal analysis is done to achieve thermal stability of the proposed system.

The paper is organized according to the following structure. Section 1 describes the overview and control of spacecrafts with electromagnetic actuators. Section 2 explains the working principle, reconfigurability and module design of Air-Coils. Section 3 describes the rotational operation of nanosatellites. Section 4 analyzes thermal operation of Air-Coils in detail and section 5 concludes the comparison of various Air-Coils configurations with commercial state of the art systems.

II. Embedded Printed Air-Coil

A. Working Principle

Printed Air-Coil can be implemented in any design configuration for small satellites but this work mainly focuses on satellites of specific dimensions. The designed printed Air-Coil unit is fully compliant with small-satellites having tile dimensions of 16×16 cm³, 13×13 cm³ and 10×10 cm³. Air-Coil is printed inside the PCB internal layers (2nd, 3rd, 4th, 5th and 6th) which is almost weightless and require no extra space and expenditure. Printed Air-Coil operates on the principle of magnetic moment ($\vec{D}$) generation as a result of current (I) passing through the Air-Coil, which is given by Eq. (1)

$$\vec{D} = N.S.I.\hat{n} \tag{1}$$

Where N is the number of turns of printed Air-Coil, S is the area of single turn and I is the current passing through it. For orientation control, Air-Coil uses the Earth magnetic field which varies with altitude and inclination angle. At an altitude of 800km and inclination angle of 89°, it varies between 0.15G and 0.45G [47]. When Earth's magnetic field ($\vec{B}$) interacts with this current carrying printed Air-Coil, a torque is generated which is given by the following equation;

$$\vec{\tau} = |\vec{D}||\vec{B}| \sin\theta\, \hat{n} \tag{2}$$

B. Reconfigurable Design

The main advantage of the designed printed Air-Coil is that one can reconfigure it according to mission requirements based on power consumption, torque, dipole moment, thermal stability and voltage & current. The design can be fully reacclimatized and made compatible with the specific spacecraft's dimensions. This Air-Coil is
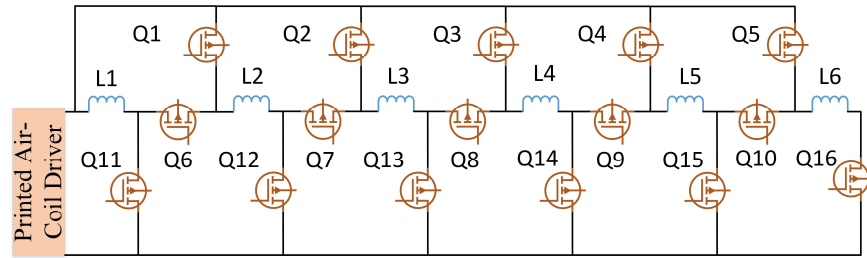

Fig. 3 Printed Air-Coils connected through switches for configurability
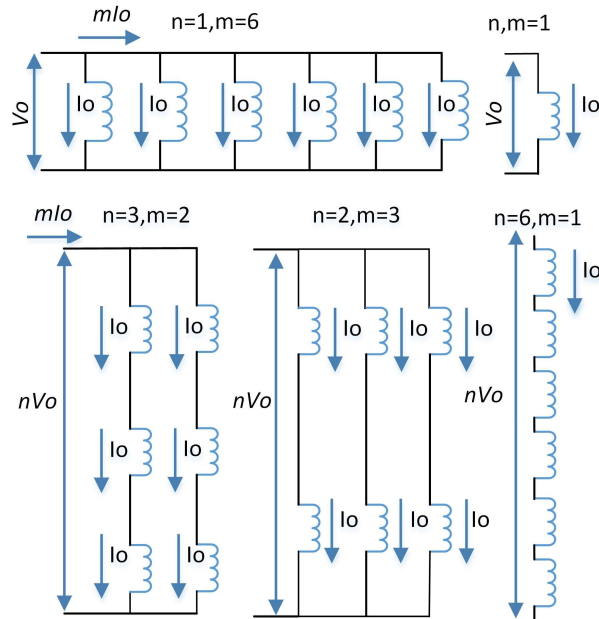

Fig. 4 Required voltages for different arrangements of coils that provide constant current

Table 1 MOSFET switches combination for different configuration of coils

S. No.	Air-Coil Configuration	ON Switches	OFF Switches
1	Single Coil	Q11.	Q1, Q2, Q3, Q4, Q5, Q6, Q7, Q8, Q9, Q10, Q12, Q14, Q15, Q16.
2	Six coils in series	Q6, Q7, Q8, Q9, Q10, Q16.	Q1, Q2, Q3, Q4, Q5, Q11, Q12, Q13, Q14, Q15.
3	Six coils in parallel	Q1, Q2, Q3, Q4, Q5, Q11, Q12, Q13, Q14, Q15, Q16.	Q6, Q7, Q8, Q9, Q10.
2	3×2 Hybrid Combination	Q6, Q7, Q13, Q3, Q9, Q10, Q16.	Q1, Q2, Q4, Q5, Q8, Q11, Q12, Q13, Q14, Q15.
4	2×3 Hybrid Combination	Q6, Q12, Q2, Q8, Q14, Q4, Q10, Q16.	Q1, Q2, Q3, Q4, Q5, Q7, Q8, Q9, Q11, Q13, Q14, Q15.

subdivided into six internal layers of the PCB with the help of transistor switches (controllable through a signal from microprocessor) or 0 Ohm resistors (mounted on PCB) which can be attached or detached. Fig. 3 shows the subcoils connected through switches for configurability. Table 1 shows the switching configuration for selecting the desired coil configuration. By readjusting the arrangement of these coils, it can be used in series, parallel or in hybrid (series-parallel) combination. In this paper the configurability aspect of the Air-Coil is tested and implemented in unit schematic design. The flexible reconfigurable design allows us to adjust the power, temperature, dipole moment and torque requirements for a specific mission.

Fig. 4 shows the printed Air-Coil possible combinations (single, n-series and m-parallel). In case of parallel configuration, to maintain a constant current (I_0) through m-parallel connected coils, the applied voltage should be the same as that of single coil (V_0). Likewise, for series configuration, the voltage is (nV_0) to pass a fixed current (I_0) through n-series connected Air-coils. For series-parallel hybrid topology, to maintain constant (I_o), the required applied voltage is (nV_0). The flexibility of this design is further explained in Air-Coil module section.

C. Printed Air-Coil Module

A fully modular, scalable, robust and diverse schematic of the designed Air Coil is shown in Fig. 5. The component selection has been done on the basis of low-cost COTS components which allows the testbed and experimental setup for private and academic institutions to indulge in small satellites research. The Air-Coil module consist of PIC microcontroller, current sensor, voltage sensor, voltage regulators, latch-up protection system, D-type connectors, Joint Test Action Group (JTAG), MOSFETs based reconfigurable circuit, differential line drivers and magnetic actuator for driving the coil.
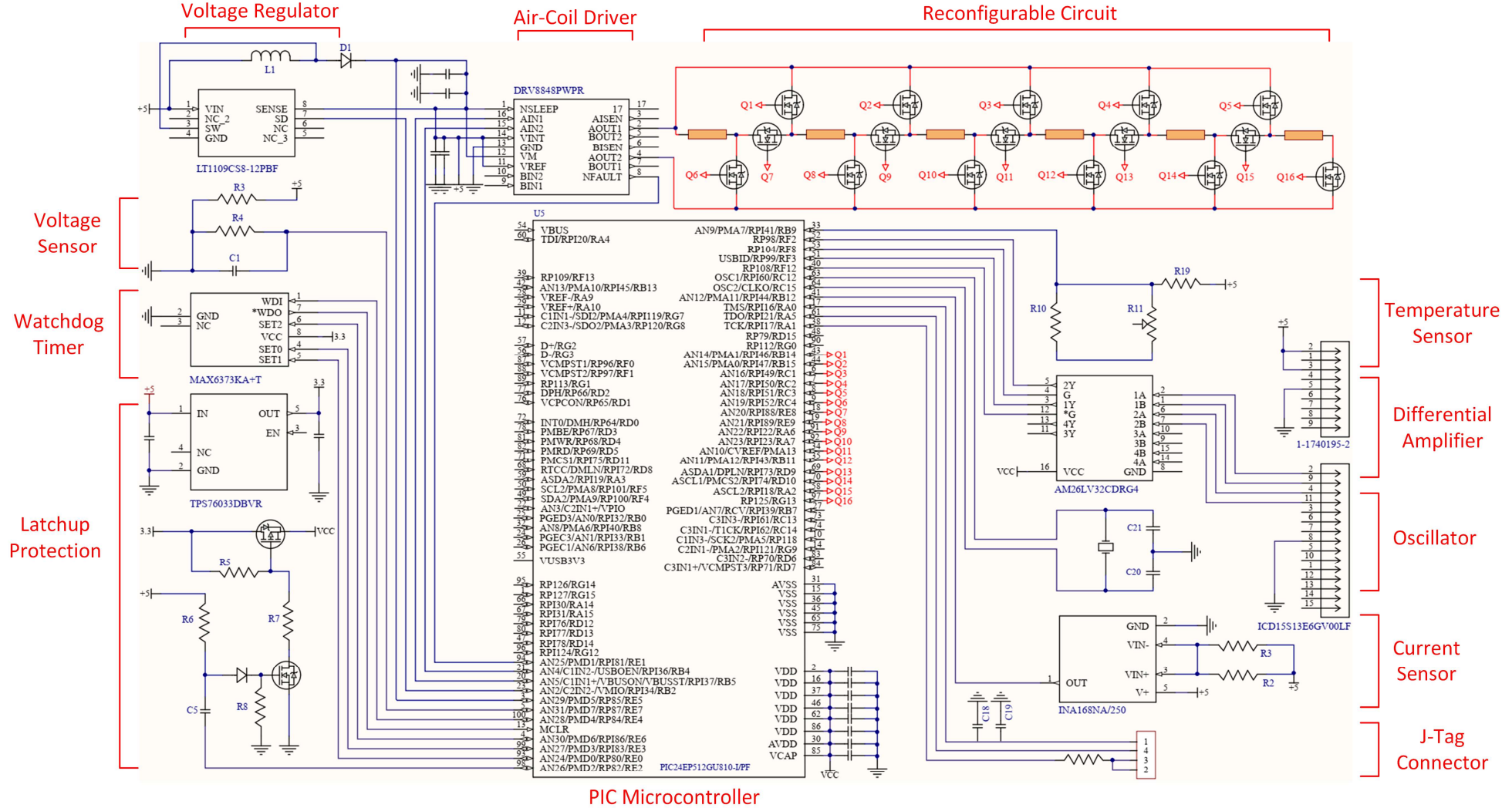
Voltage Regulator

Air-Coil Driver

Reconfigurable Circuit

L1

D1

+5

VIN SENSE
NC_2 SD
SW NC
GND NC_3

LT1109CS8-12PBF

DRV8848PWPR

NSLEEP AISEN
AIN1 AOUT1
AIN2 BOUT2
VINT BISEN
GND AOUT2
VM BOUT1
VREF NFAULT
BIN2
BIN1

Q1 Q2 Q3 Q4 Q5
Q6 Q7 Q8 Q9 Q10 Q11 Q12 Q13 Q14 Q15 Q16

Voltage Sensor

R3 +5
R4
C1

Watchdog Timer

WDI
GND *WDO
NC SET2
VCC
SETO
SET1

MAX6373KA+T

3.3

Latchup Protection

IN OUT
NC EN
GND

TPS76033DBVR

R5 VCC
+5
R6 R7
C5 R8

U5

VBUS AN9/PMA7/RPI41/RB9
TDI/RPI20/RA4 RP98/RF2
RP104/RF8
USBID/RP99/RF3
RP109/RF13 RP108/RF12
AN13/PMA10/RPI45/RB13 OSC1/RPI60/RC12
VREF-/RA9 OSC2/CLKO/RC15
VREF+/RA10 AN12/PMA11/RPI44/RB12
C1IN1-/SDO2/PMA4/RPI119/RG7 TMS/RPI16/RA0
C2IN3-/SDO2/PMA3/RPI120/RG8 TDO/RPI21/RA5
TCK/RPI17/RA1
D+/RG2 RP79/RD15
D-/RG3 RP112/RG0
VCMPST1/RP96/RF0 AN14/PMA1/RPI46/RB14
VCMPST2/RP97/RF1 AN15/PMA0/RPI47/RB15
RPI113/RG1 AN16/RPI49/RC1
DPH/RP66/RD2 AN17/RPI50/RC2
VCPCON/RP65/RD1 AN18/RPI51/RC3
AN19/RPI52/RC4
INT0/DMH/RP64/RD0 AN20/RPI88/RE8
PMBE/RP67/RD3 AN21/RPI89/RE9
PMWR/RP68/RD4 AN22/RPI22/RA6
PMRD/RP69/RD5 AN23/RPI23/RA7
PMCS1/RPI75/RD11 AN10/CVREF/PMA13
RTCC/DMLN/RPI72/RD8 AN11/PMA12/RPI43/RB11
ASDA2/RPI19/RA3 ASDA1/DPLN/RPI73/RD9
SCL2/PMA8/RP101/RF5 ASCL1/PMCS2/RPI74/RD10
SDA2/PMA9/RP100/RF4 ASCL2/RPI18/RA2
AN3/C2IN1+/VPIO RPI25/RG13
PGED3/AN0/RPI32/RB0 PGED1/AN7/RCV/RPI39/RB7
AN8/PMA6/RPI40/RB8 C3IN3-/RPI61/RC13
PGEC3/AN1/RPI33/RB1 C3IN1-/T1CK/RPI62/RC14
PGEC1/AN6/RPI38/RB6 C1IN3-/SCK2/PMA5/RPI118
VUSB3V3 C2IN1-/PMA2/RPI121/RG9
C3IN2-/RP70/RD6
C3IN1+/VCMPST3/RP71/RD7

RP126/RG14 AVSS
RP127/RG15 VSS
RPI30/RA14 VSS
RPI31/RA15 VSS
RPI76/RD12 VSS
RPI77/RD13 VSS
RPI78/RD14
RPI124/RG12
AN25/PMD1/RPI81/RE1
AN4/C1IN2-/USBOEN/RPI36/RB4
AN5/C1IN1+/VBUSON/VBUSST/RPI37/RB5 VDD
AN2/C2IN2-/VMIO/RPI34/RB2 VDD
AN29/PMD5/RP85/RE5 VDD
AN31/PMD7/RP87/RE7 VDD
AN28/PMD4/RP84/RE4 VDD
MCLR VDD
AN30/PMD6/RPI86/RE6 AVDD
AN27/PMD3/RPI83/RE3 VCAP
AN24/PMD0/RP80/RE0
AN26/PMD2/RPI82/RE2 PIC24EP512GU810-I/PF

Q1 Q2 Q3 Q4 Q5 Q6 Q7 Q8 Q9 Q10 Q11 Q12 Q13 Q14 Q15 Q16

R19 +5
R10 R11

2Y 1A
G 1B
1Y 2A
*G 2B
4Y 3A
3Y 3B
4B
4A
VCC GND

AM26LV32CDRG4

C21
C20

GND
VIN-
VIN+
OUT V+

INA168NA/250

C18 C19

Temperature Sensor
+5
1-1740195-2

Differential Amplifier

Oscillator

ICD15S13E6GV00LF

Current Sensor
R3
R2 +5

J-Tag Connector

PIC Microcontroller

Fig. 5 Air-Coil driver schematic

7

The Air-Coil unit receive 5-18V input power from the power distribution bus of the spacecraft through D-type connector [48]. 'DRV8848' [49] dual H-bridge motor driver IC is used for the magnetic actuation of the printed Air-Coil which controls the amount and direction of current flow as a function of applied voltage. The device fully supports under voltage-lockout (UVLO), short-circuit, overcurrent protection (OCP) and over temperature that makes it suitable for low earth orbit space conditions. An analog overcurrent protection limit circuit regulates current through each MOSFET by limiting gate drive. If this analog current limit remains for a duration longer than the overcurrent protection called deglitch time, the MOSFETS in the actuator are disabled and nFAULT is brought to logic level low. The device will remain disabled until the retry time occurs facilitating a very low quiescent current draw. The Air-coil is divided into six sub-coils and a reconfigurable circuit is introduced to the coil actuator 'DRV8848' IC as shown in Fig. 5 facilitating the nanosatellite with a fully modular and reconfigurable active attitude control electromagnetic printed Air-Coil. The MOSFET switches are controlled by 'DRV8848' dual H-bridge motor driver IC supervised by the tile 'PIC24' [50] microprocessor which communicates with the onboard computer (OBC) subsystem using differential line drivers though D-type connecter with its telemetries to configure coil arrangement (series, parallel or hybrid). In this way the nanosatellite is provided with the desired power, temperature, dipole moment and torque depending upon the power ratings of specific mission requirements.

A unipolar, high-Side current measurement 'INA168' [51] IC is employed that monitors the current, feeding the data to the onboard computer through telemetries. A low-cost passive temperature and voltage sensor circuits are used to monitor the Air-Coil power consumption and temperature rise within the acceptable threshold.

A watchdog 'Max6373' [52] co-processor is employed that supervise the central 'PIC24' microprocessor memory-access based activity and signals a pulse to reset the system in case of malfunctioning [53], [54]. JTAG [55] test access port is mounted which allows for testing and debugging of the Air-Coil module circuitry sufficiently to ensure proper operation [56][57].

International Geomagnetic Reference Field (IGRF) is used for magnetic field modeling [33][58]. Method of montenbruck and Pfleger [59] is used for Sun tracking modeling. The controller issues commands based on torque for required orientation according to current attitude estimation [58], [60]. The closed loop feedback ensures to maintain the required attitude control by repeating the torque command until the desired orientation is achieved.

CMOS based COTS components are susceptible to solar radiations causing latch-ups. A latch-up is an instantaneous momentary effect in which the components get short-circuited and high current passes through the

circuitry from power supply to ground that damages the system. This problem can be solved by incorporating bipolar devices in the system design because of its immunity to latch-up as they need high energy to trigger this event. But the processors are CMOS based so a latch-up protection circuit is designed and simulated according to [17] eliminating the radiation-induced latch-up in overall system [61].

The Air-Coil module has a dual redundant CAN interface using differential line drivers with OBC subsystem of nanosatellite for all telemetries and telecommands through D-type connectors. It provides sufficient telemetries (on redundant CAN interface) to monitor the power consumption of coil driver and rest of co-processors. These differential line drivers are optimized for high input impedance and high hysteresis that increase noise immunity for precise device control and accurate bus transmission at switching speeds up to 32MHz facilitating ultra-low power consumption without sacrificing speed. Fig. 6 shows Air-Coil printed inside the internal layers of the PCB.

III. Rotational Operation of Small Satellites

A. Torque Generated Vs Current Drawn

Torque exerted on the nanosatellites depends on the amount of current flow through different arrangement of coils as shown in schematic design. Air-Coil driver controls this current as a function of applied voltage. Torque generated is given by Eq. (2). For different nanosatellite dimensions, torque exerted vs current flowing in presence of 0.5G earth magnetic field through different arrangements of Air-Coil is shown in Fig. 7. Current vs torque analysis shows that
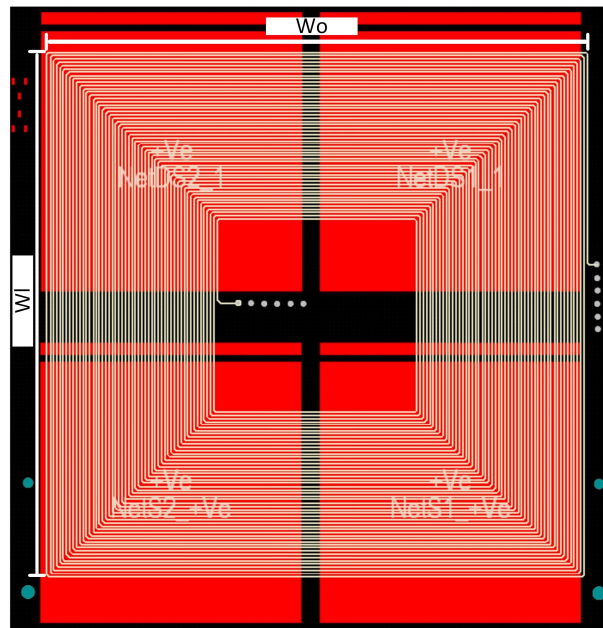

Fig. 6 Air-Coil embedded inside the internal layers

torque generated remains constant for the same current in case of six coils in series (6×1) or single coil. Torque produced for different satellites increases linearly as the dimensions of the nanosatellite increases.

B. Angular Rotation Vs Time

To align the spin axis with the Earth's inertial reference frame and stabilize the satellite, a high spin rate control is required [62]–[64]. Torque exerted and moment of inertia (J) of the nanosatellite controls the angular speed (ω) of satellite. Specific torque is required for time interval ($0 \to T/2$) to increase the satellite angular speed (ω) linearly for covering an angular distance (φ). If the nanosatellite angular speed needs to be stopped, an opposing torque of the same magnitude ($-\tau$) and duration ($T/2 \to T$) is applied. To stop the satellite at desired angular distance (φ) covered, torque should be controlled with respect to time.

According to newton's second law of rotational motion;

$$\tau = J\omega \tag{3}$$

$$\omega = \int_0^T \frac{\tau}{J} dt = \int_0^{T/2} \frac{\tau_{max}}{J} dt + \int_{T/2}^T \frac{-\tau_{max}}{J} dt$$

$$\omega = \left(\frac{\tau_{max} \cdot t}{J} \Big|_0^{T/2} ; \frac{\tau_{max} \cdot (T-t)}{J} \Big|_{T/2}^T \right) \tag{4}$$

The angular distance is given by the following equation (φ);

$$\phi = \int_0^T \omega \cdot dt = \left(\frac{\tau_{max} \cdot t^2}{2J} \Big|_0^{T/2} ; \frac{\tau_{max} \cdot T}{J} \left(t - \frac{t^2}{2T} - \frac{T}{4} \right) \Big|_{T/2}^T \right) \tag{5}$$

$$\phi = \omega \left(\frac{T}{2} \right)^2 + \omega \left(\frac{T}{2} \right)^2 = \frac{\tau}{2J} T^2$$

The time T required for the Air-Coil to revolve the satellite for required angular distance φ can be calculated from Eq. (6);

$$T = \sqrt{\frac{2J\phi}{\tau}} \tag{6}$$

Eq. (6) shows that torque applied and time required to revolve or orient the satellite are inversely related. The analysis is done for range of current inputs. The value of J is 0.0059 kgm^2, 0.0405 kgm^2 and 1.21 kgm^2 for satellites with dimensions of 10cm^3, 13cm^3 & 16cm^3 respectively. Fig. 8 shows the torque generated and the respective time
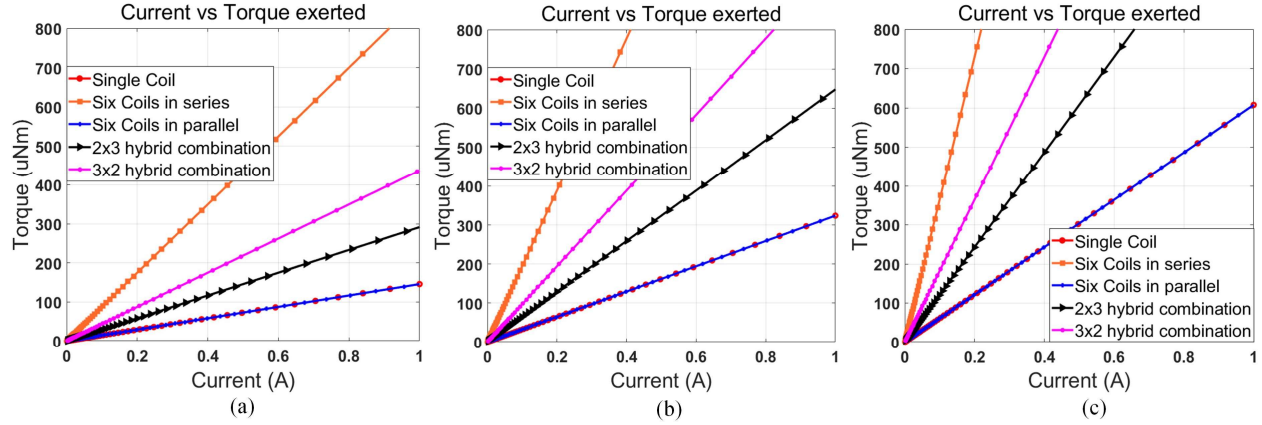
Fig. 7 Current vs Torque exerted for satellites with dimensions (a) 10×10cm³ (b) 13×13cm³ (c) 16×16cm³
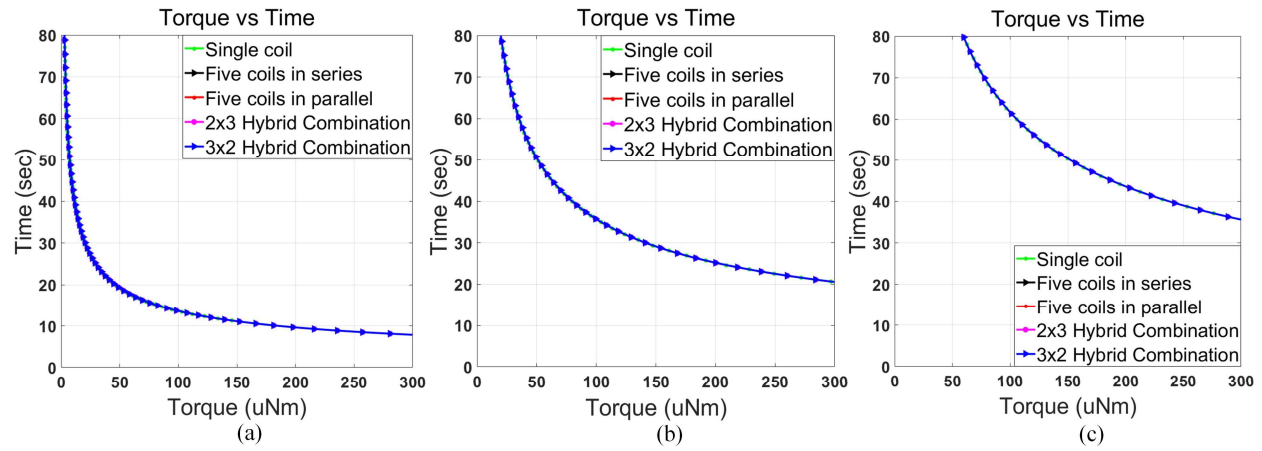
Fig. 8 Time required to rotate the satellites by an angle of 90° for satellites with dimensions (a) 10×10cm³ (b) 13×13cm³ (c) 16×16cm³

to rotate the nanosatellite at an angle of 90° by exciting various arrangements of the coils. In case of single and six coils in series, generated torque is 16.31µNm, 19.2µNm & 22.5µNm that takes 33s, 30s & 28s to spin the satellites through an angle of 90° for three nanosatellites (10cm³, 13cm³ & 16cm³) respectively. The torque generated by six coils in parallel is 98.42µNm, 110µNm & 133.4 µNm that takes 14s, 12s & 11s to rotate the satellites through an angle of 90° for three nanosatellites (10cm³, 13cm³ & 16cm³) respectively. Similarly, for hybrid (2×3) combination, torque produced is 49.9µNm, 58.7µNm & 68.1µNm that needs 19s, 17s & 16s through an angle of 90˚ rotation for three nanosatellites (10cm³, 13cm³ & 16cm³) respectively. Analysis shows that as the dimensions of satellites increases, the spinning rates subsequently increases. The maximum spinning rate is given by the parallel configuration but at the expense of high-power consumption and temperature rise.

IV. Electrothermal Analysis

The Air-Coil module is integrated with the solar panel PCB. The PCB design with the embedded printed Air-Coil is shown in Fig 9(a). The key design parameters of printed Air-Coil for various nanosatellites dimensions are represented in Table 2. In space the heat transfer takes place through conduction and no heat is transferred through convection resulting in high temperature difference between the nanosatellite surface towards the sun and bottom towards dark [65]. This temperature difference results in trapped heat inside the PCB module and rise of overall temperature which is dependent on the thermal resistance of the module. Thermal resistance is dependent on the thermal resistivity of PCB material, Air-Coil trace width & spacing and components in the selection process. Thus, thermal resistances and temperature differences needs to be calculated and modelled to illustrate thermal characteristics of the PCB for allowing the designer choose components and materials with lower thermal values. In order to get thermal resistance of the proposed design, cross sectional area of the PCB is divided into different subsections with respect to the type of material. Each subsection has the corresponding thermal resistance associated. Thermal resistance is found by using Eq. (7) [66].

$$\theta_{th} = \frac{L}{k \times S} \tag{7}$$

Where θ is the thermal resistance, L is the length, K denotes the thermal conductivity and S reflects the surface area perpendicular to heat flow.

The undesired heat power (P) translated to the system depends on the solar panel conversion efficiency (η). Greater the value of η, more power will be transformed to useful electrical power and less will be delivered as undesirable heat to the subsystem components inside the satellite. The value of P is given by Eq. (8), where 'α' denote the absorption coefficient, P_d reflects the solar power density and 'A' depicts the solar panel area exposed to solar radiations.

$$P = \alpha.p_d.A - \alpha.p_d.A.\eta. = p_d.A.(1-\eta).\alpha \tag{8}$$

If thermal resistance of solar panel PCB material is known, temperature difference 'ΔT' can be calculated from Eq. (9);

$$\Delta T = P.\theta_{th} \tag{9}$$

The Air-Coil PCB can be represented as a network of capacitors and resistors [67]. In transient thermal model, both the thermal capacitance and thermal resistance are considered and evaluated. In the steady state illustration, when the temperature and power reaches steady level, thermal capacitors are fully charged and can be neglected. Cross
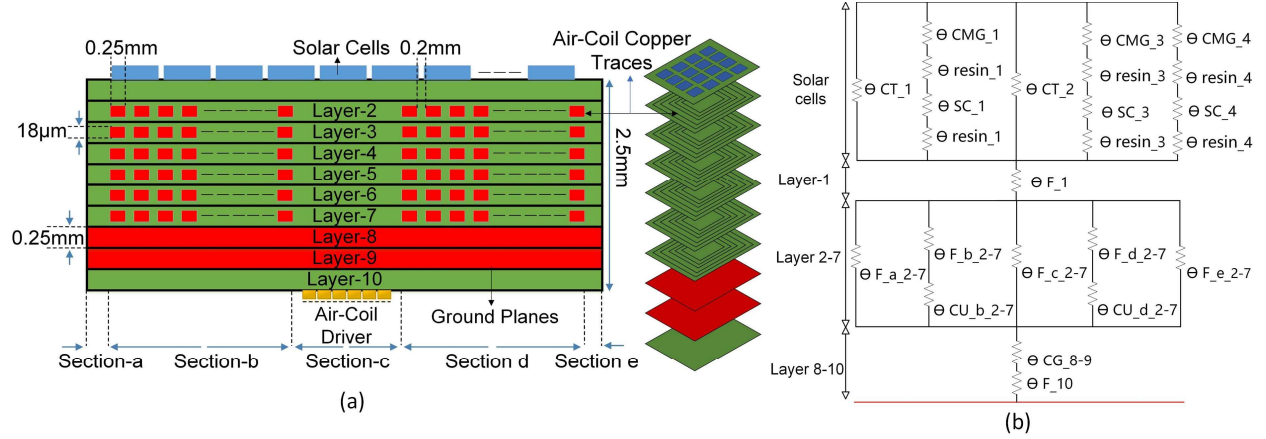
Fig. 9. (a) Cross sectional view of Air-Coil PCB. (b) Thermal resistances network of Air-Coil PCB

Table 2 Design parameters of printed Air-Coil for single layer

| Parameters	Values		
	$10cm^3$	$13cm^3$	$16cm^3$
Number of Turns, N	60	75	90
Cross sectional Area of trace, A_T	$5.4 \times 10^{-9}m^2$	$5.4 \times 10^{-9}m^2$	$5.4 \times 10^{-9}m^2$
Area occupied by single turn, A_1	$0.0036m^2$	$0.0056m^2$	$0.0081m^2$
Area occupied by single coil, A	$0.21m^2$	$0.42m^2$	$0.72m^2$
Average length of single turn, L_1	0.24 m	0.3 m	0.36 m
Average length of Single Coil, L_{avg}	14.4 m	22.5 m	32.4 m
Resistivity of copper trace, ρ	3×10^{-8} Ωm	3×10^{-8} Ωm	3×10^{-8} Ωm
Single Coil Resistance, R_1	80 ±3 Ω	125 ±3 Ω	180 ±3 Ω
Distance between two traces, T_W	0.2	0.2	0.2

Table 3 Description of parameters used in Thermal model

Parameters	Description
Θ_{CT}	Copper trace thermal resistance
Θ_{CMG}	Qouptic glass thermal resistance
Θ_{resin}	Resin thermal resistance
Θ_{SC}	Solar cell thermal resistance
Θ_{F_1}	Layer-1 FR4 material thermal resistance
$\Theta_{F\_a\_2-7}$	Thermal resistance of FR4 material in section 'a' of Layers 2, 3, 4,5,6 & 7
$\Theta_{F\_b\_2-7}$	Thermal resistance of FR4 material in section 'b' of Layers 2, 3, 4,5,6 & 7
$\Theta_{F\_e\_2-7}$	Thermal resistance of FR4 material in section 'e' of Layers 2, 3, 4,5,6 & 7
$\Theta_{Cu\_b\_2-7}$	Thermal resistance of copper material in section 'b' of Layers 2, 3, 4,5,6 & 7
$\Theta_{Cu\_d\_2-7}$	Thermal resistance of copper material in section 'd' of Layers 2, 3, 4,5,6 & 7
Θ_{CG_8-9}	Thermal resistance of copper ground material in Layers 8 & 9
Θ_{F_10}	Thermal resistance of FR4 material in Layer 10

sectional view of solar cells mounted on the top layer and Air-Coil driver on the bottom layer is shown in Fig 9(a). Solar cells are mounted on Layer-1 (top layer) composed of FR4 material with thermally conductive resin, while layers-2, 3, 4, 5, 6 and 7 have copper traces of Air-Coil inserted in FR4 material. Layers-8 and 9 have copper ground planes embedded in FR4 material while layer-10 (bottom layer) has FR4 material. Each layer has a thickness of 0.25mm. Copper traces and ground planes have thickness of 18μm. Width of the copper traces is 0.25mm. The PCB is divided into subsections with respect to the type of material. Depending on the type of material each subsection has a corresponding thermal resistance. The thermal resistance value is dependent on the material type, length and width of parameters. Subscript notations are depicted in Table 3. θ represents the thermal resistance of the material used. F denotes FR4, Cu represent copper, the alphabet letters (*a, b, c, d, e*) denote the respective subsections, and numbers (*1, 2, 3, 4*) describe the respective layers. For example, $\theta_{F_{a-2,3,4,5,7}}$ denote thermal resistance of FR4 material in subsection '*a*' of layers *2, 3, 4, 5, 6 & 7*. Table 3 gives description of the parameters used in illustrating the thermal resistance. Cross sectional view of Air-Coil module from Fig. 9(a) is represented as network of thermal resistances in Fig. 9(b). Thermal resistance network of the Air-Coil PCB is mathematically represented in Eq. (10). Thermal resistance of the Air-Coil module can be calculated by putting length, width and conductivity values of PCB different sections into Eq. (7). Thermal resistance of the Air-Coil module for 10cm^3, 13cm^3 & 16cm^3 satellites are 0.006 K/W, 0.005 K/W and 0.0039K/W respectively. For solar radiation intensity level of 1365W/m² at the solar panel module, the respective temperature differences are 8.64K, 7.02K and 5.4K for 10cm^3, 13cm^3 & 16cm^3 satellites respectively. The temperature differences of the respective Air-Coil PCBs between the top and bottom surface of the Air-Coil module show a subsequent decrease as the dimensions of satellites increase.

$$\theta_{th} = \frac{\theta_{ct}}{4} \, || \left(\frac{\theta_{CMG} + 2\theta_{resin+\theta_{SC}}}{2} \right) + \theta_{F_1} + [\theta_{F_{a_{2,3,4,5,6,7}}} || (\theta_{F_{b_{2,3,4,5,6,7}}} + \theta_{Cu_{2,3,4,5,6,7}})$$

$$|| \theta_{F_{c_{2,3,4,5,6,7}}} || (\theta_{F_{d_{2,3,4,5,6,7}}} + \theta_{Cu_{2,3,4,5,6,7}}) \, || \, \theta_{F_{e_{2,3,4,5,6,7}}}] + \theta_{CG_{8,9}} + \theta_{F_{10}} \qquad (11)$$

V. Comparison of Air-Coil Configurations

Comparative analyses for satellites with dimensions $10cm^3$, $13cm^3$ and $16cm^3$ have been done on the basis of thermal stability, magnetic moment generated, power dissipation and resultant torque as shown in Fig. 11-13. Power consumption and thermals are analyzed by measuring the amount of current that flows through the Air-Coils. Current flowing through the printed Air-Coils is responsible for magnetic moment generation which in turn gives rise to the
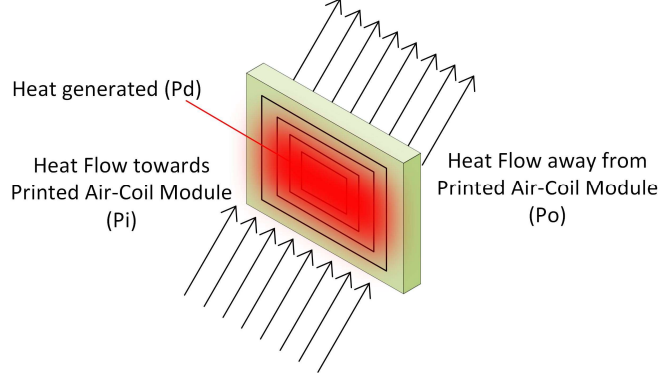
Fig. 10. Heat flow through the solar panels with embedded Air-Coils

temperature of the module. Thus, temperature and magnetic moment are coherent parameters. Greater magnetic moment can be acquired but at the cost of higher solar panel module temperature.

This rise in temperature should be investigated to ensure thermal balance of the system within allowable limits to avoid thermal failures that may compromise system's safety. In case of thermal equilibrium, the total dissipative power from the solar panel unit to the surroundings (P_o) is equivalent to the electrical power consumed by the coil (P_d) inside the PCB and power absorbed from the surroundings (P_I) as depicted in Fig 10 and given in Eq. (11);

$$P_o = P_d + P_I \tag{11}$$

The power dissipated by M coils can be calculated from the Stefan-Boltzmann's law [68]

$$P_o = \alpha_o \sigma T_o{}^4 S \tag{12}$$

Where σ denote the Stefan-Boltzmann constant.

T_0 reflects the solar panel unit surface temperature in Kelvin.

S represent both sides of solar panel unit surface area.

α_0 is the emissivity of the Air-Coil PCB material at radiated wavelength.

Eq. (11) and (12) result in Eq. (13);

$$\alpha_o \sigma T_o{}^4 S = P_d + P_I \tag{13}$$

when thermal equilibrium is attained, no current passes through the coil, $P_{d\,=}\,0$, and Eq. (13) results in the following equation;

$$\alpha_I \sigma T_I{}^4 S = P_I \tag{14}$$

Where α_I is the emissivity of the solar panel unit surface for the heat absorption wavelength λ_I. Using P_I value from Eq. (14) and putting into Eq. (13) result in Eq. (15);
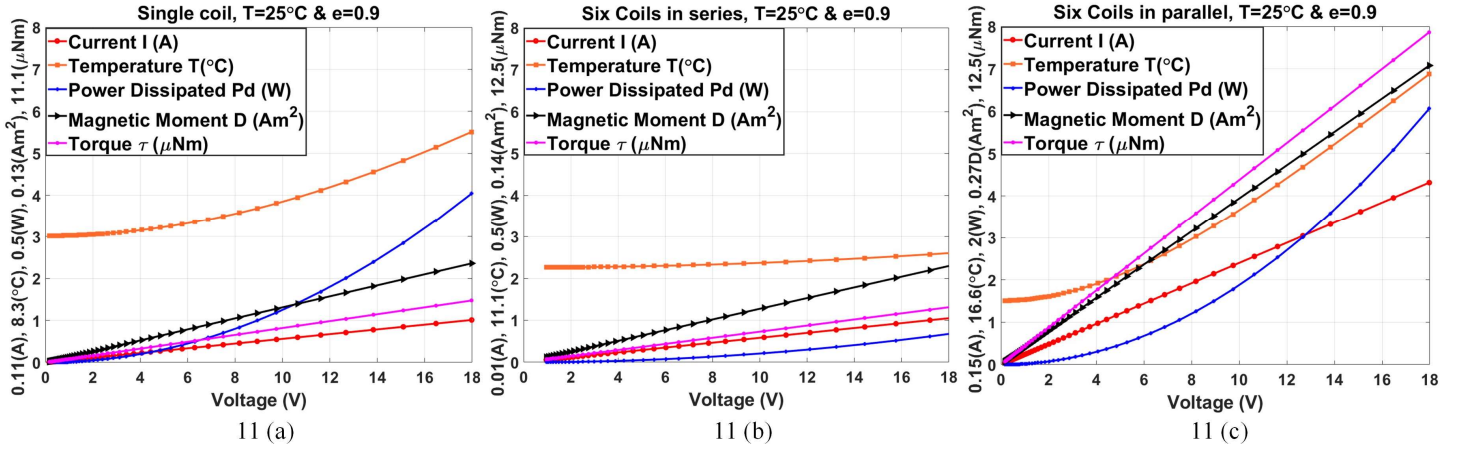
Fig. 11: $10 \times 10 \text{cm}^3$ Nanosatellite ;Plots of current, magnetic moment, power dissipated and temperature against applied voltage for (a) Single coil (b) Six coils connected in series (c) Six coils connected in parallel (d) 2x3 hybrid combination (e) 3x2 hybrid combination

Fig. 12: $13 \times 13 \text{cm}^3$ Nanosatellite ;Plots of current, magnetic moment, power dissipated and temperature against applied voltage for (a) Single coil (b) Six coils connected in series (c) Six coils connected in parallel (d) 2x3 hybrid combination (e) 3x2 hybrid combination
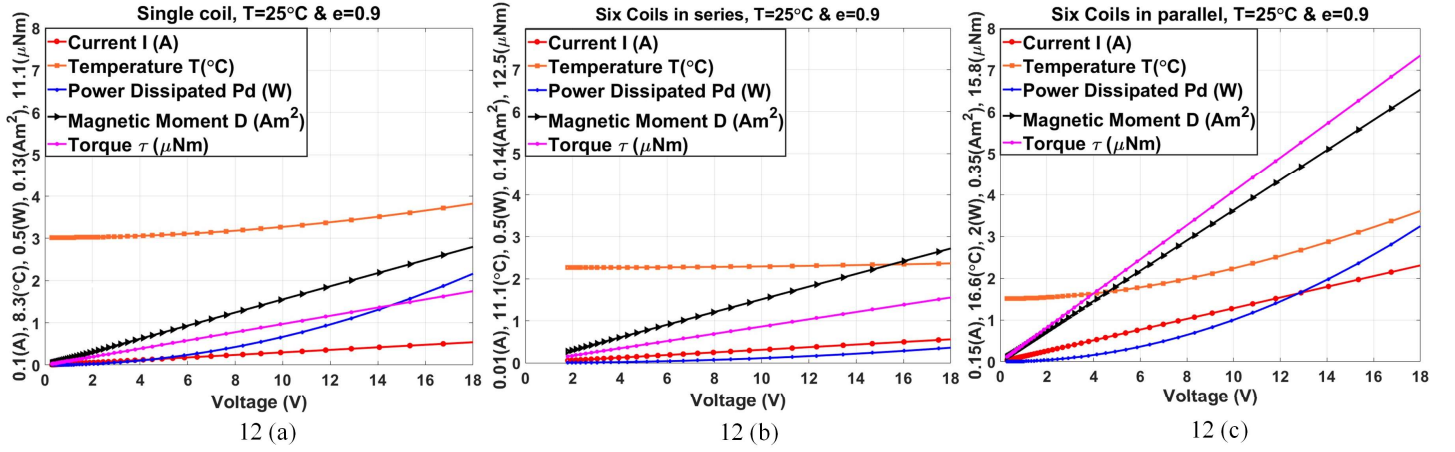
Fig. 13: 10x10cm³ Nanosatellite ;Plots of current, magnetic moment, power dissipated and temperature against applied voltage for (a) Single coil (b) Six coils connected in series (c) Six coils connected in parallel (d) 2x3 hybrid combination (e) 3x2 hybrid combination
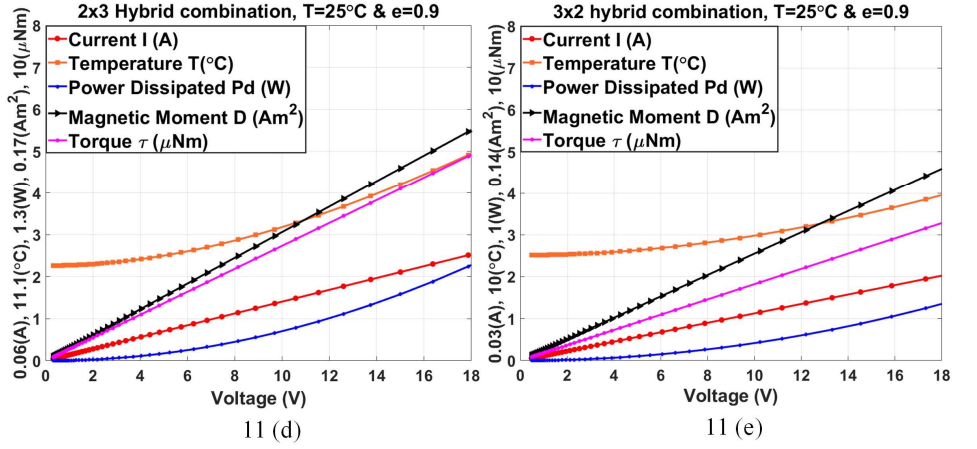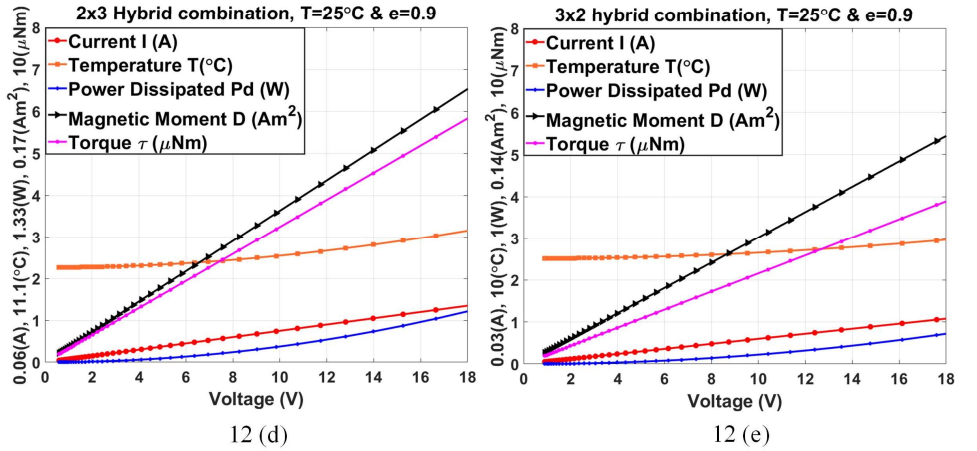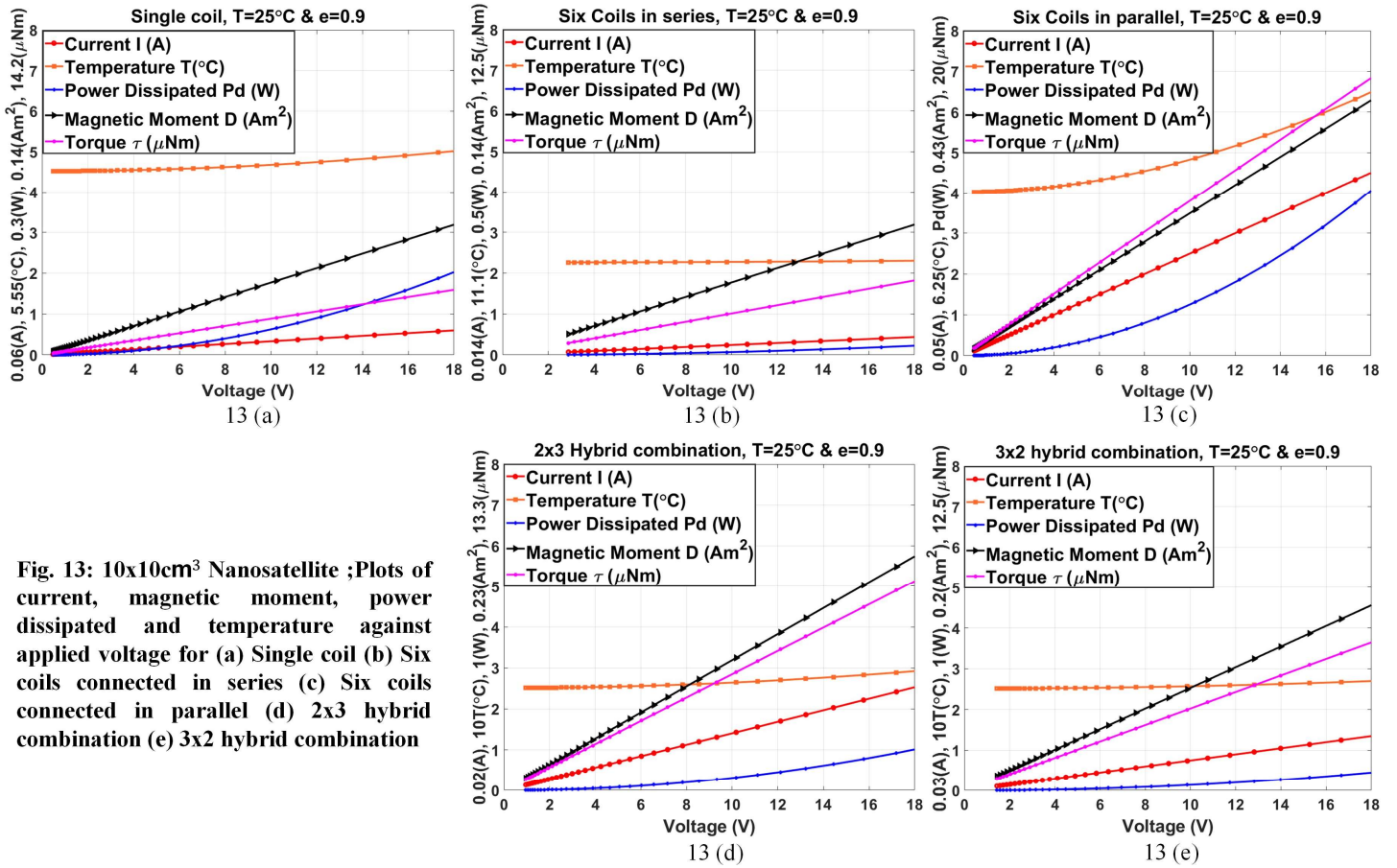
Table 4 Comparison of printed Air-Coil with other commercial state of the art designs

Attitude control System		Price	Mass (g), +/- 0.25g	Dimensions (mm)	P (W)	τ (μNm)	μ (Am²)	$\dfrac{\tau}{P}$
Commercial Designs	CubeTorquer and CubeCoil [69]	$1850	27.5	60(L) ×10(ϕ)	10.8	12	0.24	1.1
			45.9	90 × 96 × 6	3.95	7	0.13	1.7
	Gomspace Nanopower P110 [70]	Internal to the PCB (No extra price)	Almost massless	Internal to PCB	3.3	1.90	0.038	0.2
	NCTR-M012 Magnetorquer Rod [71]	$2000	50 g	94 × 15 × 13	2.88	60	1.2	20.8
Embedded Printed Air-coil	Six coils in series (6×1)	Internal to the PCB (No extra price)	Almost massless	Internal to PCB	0.36	16.31	0.99	45.3
	Six coils in parallel (1×6)	Internal to the PCB (No extra price)	Almost massless	Internal to PCB	12.09	98.42	1.97	8.2

$$\alpha_o \sigma T_o{}^4 S = P_o + \alpha_I \sigma T_I{}^4 S \qquad (15)$$

In thermal equilibrium, $\alpha_0 = \alpha_I = \alpha$. Solving Eq. (15) further will give a relation between P_o and T_o as given in Eq. (16);

$$T_o = \sqrt[4]{\frac{P_d + \alpha \sigma T_I{}^4 S}{\alpha \sigma S}} \qquad (16)$$

The value of emissivity (α) as given in Eq. (16) is required to find the relation between P_o and T_o.

$$\alpha = \frac{P_d}{\sigma S (T_o{}^4 - T_I{}^4)} \qquad (17)$$

The power dissipated (P_d) by the air-coil is represented by Eq. (18), where I is the current passing through the air-coil with resistance R;

$$P_d = I^2 R \qquad (18)$$

The surface emissivity ($\alpha = 0.9$) value of solar panel module is found in [43] by conducting a laboratory experiment. This emissivity value is used for the calculation of T_o in case of different configuration of the Air-Coils.

Thermal analysis for the Air-Coil PCB module shows that the increase in the number of turns, trace widths, trace thickness and material used have significant dependence on the temperature rise of the PCB. The current rating of different configurations depends upon the resistance of the respective coils. It can be noticed, by increasing the dimensions of nanosatellites, magnetic moment and torque generation increases with the corresponding decrease in temperature and power dissipation.

The analysis is done for range of 18V inputs applied to satellites with dimensions $10\text{cm}^3, 13\text{cm}^3$ & 16cm^3 as shown in Fig 11-13. In case of six coils in series (6×1), the resulting current is 18mA, 9mA & 6mA, dissipated power is 0.36W, 0.17W & 0.11W, magnetic moment generated is $0.3\text{Am}^2, 0.37\text{Am}^2$ & 0.45Am^2, PCB temperature rise to 30°C, 26.5°C & 25°C and generated torque is 16.31µNm, 19.2µNm & 22.5µNm for three satellites ($10\text{cm}^3, 13\text{cm}^3$ & 16cm^3) respectively. In case of hybrid combination (2×3), the corresponding current is 167mA, 90mA & 50mA, dissipated power is 2.99W, 1.64W & 1.05W, magnetic moment generated is $0.99\text{Am}^2, 1.17\text{Am}^2$ & 1.36Am^2, torque produced is 49.9µNm, 58.7µNm & 68.1µNm and PCB temperature rise to 54.51°C, 35.2°C & 29.2°C for three satellites ($10\text{cm}^3, 13\text{cm}^3$ & 16cm^3) respectively. Similarly, using parallel configuration, the corresponding current is 674mA, 365mA & 230mA, dissipated power is 12W, 6.6W & 3.8W, magnetic moment generated is 1.97Am^2,

2.35Am^2 & 2.7Am^2, torque produced is 98.42µNm, 110µNm & 133.4µNm and PCB temperature rise to 115˚C, 60.2˚C & 40.1˚C for three satellites (10cm^3, 13cm^3 & 16cm^3) respectively.

Fig 11(b), 12(b) and 13(b) shows the optimized printed Air-Coil with configuration six coils in series gives the maximum torque vs power dissipation ratio for all the nanosatellites. The maximum temperature rise of 115˚C is given by 6 coils in parallel for 10cm^3 nanosatellite in Fig 11(c). It is the temperature at the steady state when the coil is energized for longer period of time. Also, as mentioned before in section 3, the maximum torque generated by six coils in parallel is 98.42µNm that takes 14 seconds for 90˚ rotation which shows that the temperature rise of the module due to excitation of the embedded coils is very low and the coils will be excited at most once a week that will not harm the operations of other subsystems. It can be noticed that as the dimensions of nanosatellites increases the temperature and power dissipation also subsequently decreases which shows the coils direct dependence on size, trace width and spacing in the module. The analysis show that the overall temperature of coils increases at higher operating voltages but remains well within the thermal limits even for the worst case of six coils in parallel configuration. Therefore, lower operating voltages for the printed Air-Coil sustain better thermal operation as a design selection. Table 4 shows the comparison of optimized printed Air-Coil with other commercial state of the art designs available in market. The Air-Coil with additional configurability features (2×3, 3×2 hybrid) provides more flexibility to the design aspects by changing the arrangement through the onboard processor. Depending upon the mission requirements, data from telemetry points are sent to the OBC and telemetry processor unit for transmission to ground station for required power consumption, torque or dipole moment generated by the coil.

VI. Conclusion

An innovative design of electromagnetic embedded printed Air-Coil for nanosatellites was proposed to achieve the desired magnetic dipole moment and torque produced. The design is made fully reconfigurable to offer more flexibility according to power requirements and can be reused for multiple missions. The optimized reconfigurable design was compared with the commercially available designs. Commercial NCTR-M012 magnetorquer rod provides good magnetic moment versus power ratio but it is expensive, heavier and occupy extra space on the vehicle which is not suitable for 1U based nanosatellites. Gomspace Nano Power p110U like proposed Air-Coil is internal to PCB but offers very weak torque to power dissipation ratio. The proposed printed Air-coil with configuration of six coils (6×1) in series gives the maximum torque vs power ratio. Thermal analyses were done in detail to ensure the feasibility and

merit of the proposed embedded Air-Coil. Future work can be done on the presented coil configurations for higher form factor commercial microsatellites.

References

[1]   E. Mazareanu, "Number of satellites in orbit by country as of 2019," 2020. https://www.statista.com/statistics/264472/number-of-satellites-in-orbit-by-operating-country/ (accessed Jun. 03, 2020).

[2]   G. Liu and S. Zhang, "A Survey on Formation Control of Small Satellites," *Proc. IEEE*, vol. 106, no. 3, pp. 440–457, 2018, doi: 10.1109/JPROC.2018.2794879.

[3]   M. N. Sweeting, "Modern Small Satellites-Changing the Economics of Space," *Proc. IEEE*, vol. 106, no. 3, pp. 343–361, 2018, doi: 10.1109/JPROC.2018.2806218.

[4]   M. O'Halloran, J. G. Hall, and L. Rapanotti, "Safety engineering with COTS components," *Reliab. Eng. Syst. Saf.*, vol. 160, pp. 54–66, 2017, doi: https://doi.org/10.1016/j.ress.2016.11.016.

[5]   S. Dahbi *et al.*, "Power budget analysis for a LEO polar orbiting nano-satellite," in *2017 International Conference on Advanced Technologies for Signal and Image Processing (ATSIP)*, 2017, pp. 1–6, doi: 10.1109/ATSIP.2017.8075580.

[6]   D. Selčan, G. Kirbiš, and I. Kramberger, "Nanosatellites in LEO and beyond: Advanced Radiation protection techniques for COTS-based spacecraft," *Acta Astronaut.*, 2017, doi: 10.1016/j.actaastro.2016.11.032.

[7]   P. B. Guldager, G. G. Thuesen, and J. L. Jørgensen, "Quality assurance for space instruments built with COTS," in *Acta Astronautica*, 2005, doi: 10.1016/j.actaastro.2004.09.024.

[8]   I. D. Moscholios, V. G. Vassilakis, N. C. Sagias, and M. D. Logothetis, "On Channel Sharing Policies in LEO Mobile Satellite Systems," *IEEE Trans. Aerosp. Electron. Syst.*, 2018, doi: 10.1109/TAES.2018.2798318.

[9]   A. Ali, S. A. Khan, M. A. Dildar, H. Ali, and N. Ullah, "Design & thermal modeling of solar panel module with embedded reconfigurable Air-Coil for micro-satellites," *PLoS One*, 2018, doi: 10.1371/journal.pone.0199145.

[10]   D. Selva, A. Golkar, O. Korobova, I. L. i Cruz, P. Collopy, and O. L. de Weck, "Distributed Earth Satellite Systems: What Is Needed to Move Forward?," *J. Aerosp. Inf. Syst.*, vol. 14, no. 8, pp. 412–438, Aug. 2017, doi: 10.2514/1.I010497.

[11]   S. Spangelo and J. Cutler, "Analytical Modeling Framework and Applications for Space Communication

Networks," *J. Aerosp. Inf. Syst.*, vol. 10, no. 10, pp. 452–466, Oct. 2013, doi: 10.2514/1.I010086.

[12] A. K. Kennedy and K. L. Cahoy, "Performance Analysis of Algorithms for Coordination of Earth Observation by CubeSat Constellations," *J. Aerosp. Inf. Syst.*, vol. 14, no. 8, pp. 451–471, Oct. 2016, doi: 10.2514/1.I010426.

[13] P. C. Lusk, P. C. Glaab, L. J. Glaab, and R. W. Beard, "Safe2Ditch: Emergency Landing for Small Unmanned Aircraft Systems," *J. Aerosp. Inf. Syst.*, vol. 16, no. 8, pp. 327–339, Jul. 2019, doi: 10.2514/1.I010706.

[14] S. H. Kim, "Third-Party Risk Analysis of Small Unmanned Aircraft Systems Operations," *J. Aerosp. Inf. Syst.*, vol. 17, no. 1, p. 24, Oct. 2019, doi: 10.2514/1.I010763.

[15] E. Kulu, "Nanosatellites by organizations," 2020. https://www.nanosats.eu/cubesat (accessed Mar. 06, 2020).

[16] A. K. Maini and V. Agrawal, *Satellite Technology: Principles and Applications: Third Edition*. 2014.

[17] A. Ali, S. A. Khan, M. Usman Khan, H. Ali, M. Rizwan Mughal, and J. Praks, "Design of modular power management and attitude control subsystems for a microsatellite," *Int. J. Aerosp. Eng.*, 2018, doi: 10.1155/2018/2515036.

[18] A. M. Zanchettin, A. Calloni, and M. Lovera, "Robust magnetic attitude control of satellites," *IEEE/ASME Trans. Mechatronics*, 2013, doi: 10.1109/TMECH.2013.2259843.

[19] R. C. Leishman and T. W. McLain, "Multiplicative Extended Kalman Filter for Relative Rotorcraft Navigation," *J. Aerosp. Inf. Syst.*, vol. 12, no. 12, pp. 728–744, Dec. 2014, doi: 10.2514/1.I010236.

[20] P. Z. Schulte and D. A. Spencer, "State Machine Fault Protection Architecture for Aerospace Vehicle Guidance, Navigation, and Control," *J. Aerosp. Inf. Syst.*, vol. 17, no. 2, pp. 70–85, Dec. 2019, doi: 10.2514/1.I010673.

[21] Z.-F. Gao, B. Jiang, P. Shi, and Y.-H. Cheng, "Sensor fault estimation and compensation for microsatellite attitude control systems," *Int. J. Control. Autom. Syst.*, vol. 8, no. 2, pp. 228–237, 2010, doi: 10.1007/s12555-010-0207-7.

[22] J. Li, M. Post, T. Wright, and R. Lee, "Design of attitude control systems for CubeSat-class nanosatellite," *J. Control Sci. Eng.*, 2013, doi: 10.1155/2013/657182.

[23] M. Lovera, E. De Marchi, and S. Bittanti, "Periodic attitude control techniques for small satellites with magnetic actuators," *IEEE Trans. Control Syst. Technol.*, 2002, doi: 10.1109/87.974341.

[24] L. Sun, Z. Wang, G. Zhao, and H. Huang, "Magnetic attitude tracking control of gravity gradient microsatellite

in orbital transfer," *Aeronaut. J.*, 2019, doi: 10.1017/aer.2019.112.

[25] M. Y. Ovchinnikov and V. I. Penkov, "Passive magnetic attitude control system for the munin nanosatellite," *Cosm. Res.*, 2002, doi: 10.1023/A:1015197303662.

[26] M. Y. Ovchinnikov, V. D. Shargorodskiy, V. I. Pen'kov, S. A. Mirer, A. D. Guerman, and R. B. Nemuchinskiy, "Nanosatellite REFLECTOR: Choice of parameters of the attitude control system," *Cosm. Res.*, 2007, doi: 10.1134/S0010952507010078.

[27] F. Santoni and M. Zelli, "Passive magnetic attitude stabilization of the UNISAT-4 microsatellite," *Acta Astronaut.*, 2009, doi: 10.1016/j.actaastro.2009.03.012.

[28] L. Lorello *et al.*, "Hall Thrusters with Permanent Magnets: Current Solutions and Perspectives," *IEEE Trans. Plasma Sci.*, 2018, doi: 10.1109/TPS.2017.2772332.

[29] D. Yongjie, P. Wuji, W. Liqiu, S. Guoshun, L. Hong, and Y. Daren, "Computer simulations of Hall thrusters without wall losses designed using two permanent magnetic rings," *J. Phys. D. Appl. Phys.*, 2016, doi: 10.1088/0022-3727/49/46/465001.

[30] Y. Raitses, D. Staack, A. Dunaevsky, and N. J. Fisch, "Operation of a segmented Hall thruster with low-sputtering carbon-velvet electrodes," *J. Appl. Phys.*, 2006, doi: 10.1063/1.2168023.

[31] K. D. Kumar, M. J. Tahk, and H. C. Bang, "Satellite attitude stabilization using solar radiation pressure and magnetotorquer," *Control Eng. Pract.*, 2009, doi: 10.1016/j.conengprac.2008.07.006.

[32] V. Francois-Lavet, "Study of passive and active attitude control systems for the OUFTI nanosatellites," *Math. Model.*, 2010.

[33] C. C. Finlay *et al.*, "International Geomagnetic Reference Field: The eleventh generation," *Geophys. J. Int.*, 2010, doi: 10.1111/j.1365-246X.2010.04804.x.

[34] M. Y. Ovchinnikov and D. S. Roldugin, "A survey on active magnetic attitude control algorithms for small satellites," *Progress in Aerospace Sciences*. 2019, doi: 10.1016/j.paerosci.2019.05.006.

[35] H. Leeghim, H. Bang, and C.-Y. Lee, "Angular Rate and Alignment Estimation for Gyroless Spacecraft by Only Star Trackers," *Int. J. Control. Autom. Syst.*, vol. 16, no. 5, pp. 2235–2243, 2018, doi: 10.1007/s12555-017-0750-6.

[36] S. S.-M. Swei and N. T. Nguyen, "Adaptive Disturbance Torque Estimation for Orbiting Spacecraft Using Recursive Least-Squares Methods," *J. Aerosp. Inf. Syst.*, vol. 14, no. 2, pp. 92–102, Dec. 2016, doi:

10.2514/1.I010480.

[37] J. Wertz and H. Wittenberg, "Book-Review - Spacecraft Attitude Determination and Control," *Space Sci. Rev.*, 1979.

[38] J. F. Trégouët, D. Arzelier, D. Peaucelle, C. Pittet, and L. Zaccarian, "Reaction wheels desaturation using magnetorquers and static input allocation," *IEEE Trans. Control Syst. Technol.*, 2015, doi: 10.1109/TCST.2014.2326037.

[39] D. V. Lebedev, "Momentum unloading excessive reaction-wheel system of a spacecraft," *J. Comput. Syst. Sci. Int.*, 2008, doi: 10.1134/S1064230708040138.

[40] P. J. Camillo and F. L. Markley, "Orbit-averaged behavior of magnetic control laws for momentum unloading," *J. Guid. Control. Dyn.*, 1980, doi: 10.2514/3.19725.

[41] R. J. MCELVAIN, "Satellite Angular Momentum Removal Utilizing the Earth's Magnetic Field," in *Applied Mathematics and Mechanics*, Elsevier Inc., 1964, pp. 137–158.

[42] M. J. Sidi, *Spacecraft dynamics and control: A practical engineering approach*. 2014.

[43] A. Ali, M. R. Mughal, H. Ali, L. M. Reyneri, and M. N. Aman, "Design, implementation, and thermal modeling of embedded reconfigurable magnetorquer system for nanosatellites," *IEEE Trans. Aerosp. Electron. Syst.*, 2015, doi: 10.1109/TAES.2015.130621.

[44] E. L. De Angelis, F. Giulietti, A. H. J. De Ruiter, and G. Avanzini, "Spacecraft attitude control using magnetic and mechanical actuation," *J. Guid. Control. Dyn.*, 2016, doi: 10.2514/1.G000957.

[45] F. Celani, "Spacecraft attitude stabilization using magnetorquers with separation between measurement and actuation," *J. Guid. Control. Dyn.*, 2016, doi: 10.2514/1.G001804.

[46] D. Ivanov, M. Ovchinnikov, and D. Roldugin, "Three-axis attitude determination using magnetorquers," *J. Guid. Control. Dyn.*, 2018, doi: 10.2514/1.G003698.

[47] SPENVIS, "Space Enivornment Information System," 2020. https://www.spenvis.oma.be/ (accessed Apr. 03, 2020).

[48] DS-9, "D-type Connector," *Molex*. https://www.molex.com/pdm_docs/sd/836129024_sd.pdf (accessed Jun. 05, 2020).

[49] DRV8848, "Motor Drive and Control Solutions," *Texas Instruments*. http://www.ti.com/lit/pdf/slyb165 (accessed Jun. 03, 2020).

[50]   PIC24, "16-bit Embedded Control Solutions," *Microchip Technology*. http://ww1.microchip.com/downloads/en/DeviceDoc/00001032T.pdf (accessed Jun. 05, 2020).

[51]   INA168, "Current Shunt Monitor," *Texas Instruments*. http://www.ti.com/general/docs/suppproductinfo.tsp?distId=10&gotoUrl=http%3A%2F%2Fwww.ti.com%2F Flit%2Fgpn%2Fina138 (accessed Jun. 03, 2020).

[52]   Max6373, "IC supervisor," *Integrated Maxim*. https://datasheets.maximintegrated.com/en/ds/MAX6369-MAX6374.pdf (accessed Jun. 05, 2020).

[53]   A. Rajabzadeh and S. G. Miremadi, "A hardware approach to concurrent error detection capability enhancement in COTS processors," in *Proceedings - 11th Pacific Rim International Symposium on Dependable Computing, PRDC 2005*, 2005, doi: 10.1109/PRDC.2005.7.

[54]   A. Mahmood and E. J. Mccluskey, "Concurrent Error Detection Using Watchdog Processors—A Survey," *IEEE Trans. Comput.*, 1988, doi: 10.1109/12.2145.

[55]   PicoBlade, "PCB headers," *Molex*. https://www.molex.com/molex/products/part-detail/pcb_headers/0533980467 (accessed Jun. 04, 2020).

[56]   K. Rosenfeld and R. Karri, "Attacks and defenses for JTAG," *IEEE Des. Test Comput.*, 2010, doi: 10.1109/MDT.2010.9.

[57]   V. N. Be, P. Law, and A. Sparks, "Use of JTAG boundary-scan for testing electronic circuit boards and systems," in *AUTOTESTCON (Proceedings)*, 2008, doi: 10.1109/AUTEST.2008.4662576.

[58]   S. G. Kim, J. L. Crassidis, Y. Cheng, A. M. Fosbury, and J. L. Junkins, "Kalman filtering for relative spacecraft attitude and position estimation," *J. Guid. Control. Dyn.*, 2007, doi: 10.2514/1.22377.

[59]   O. Montenbruck and T. Pfleger, *Astronomy on the Personal Computer*. 2000.

[60]   A. Slavinskis *et al.*, "Flight results of ESTCube-1 attitude determination system," *J. Aerosp. Eng.*, 2016, doi: 10.1061/(ASCE)AS.1943-5525.0000504.

[61]   B. L. Gregory and B. D. Shafer, "Latch-Up in CMOS Integrated Circuits," *IEEE Trans. Nucl. Sci.*, vol. 20, no. 6, pp. 293–299, 1973, doi: 10.1109/TNS.1973.4327410.

[62]   H. Ehrpais, J. Kütt, I. Sünter, E. Kulu, A. Slavinskis, and M. Noorma, "Nanosatellite spin-up using magnetic actuators: ESTCube-1 flight results," *Acta Astronaut.*, 2016, doi: 10.1016/j.actaastro.2016.07.032.

[63]   A. Slavinskis *et al.*, "High spin rate magnetic controller for nanosatellites," *Acta Astronaut.*, 2014, doi:

10.1016/j.actaastro.2013.11.014.

[64]   F. Zhang and G.-R. Duan, "Manipulator-actuated Adaptive Integrated Translational and Rotational Stabilization for Spacecraft in Proximity Operations with Control Constraint," *Int. J. Control. Autom. Syst.*, vol. 16, no. 5, pp. 2103–2113, 2018, doi: 10.1007/s12555-017-0689-7.

[65]   J. Meseguer, I. Pérez-Grande, and A. Sanz-Andrés, "Thermal radiation heat transfer," in *Spacecraft Thermal Control*, 2012.

[66]   I. R. Fort Collins, "Thermal Resistance and Power Dissipation, Technical Note on Calculation of R Theta and Power Dissipation," *thermal resistance and power dissipation calculation in semiconductors.* Colorado, 2003.

[67]   S. Armstrong and W. G. Hurley, "A thermal model for photovoltaic panels under varying atmospheric conditions," *Appl. Therm. Eng.*, 2010, doi: 10.1016/j.applthermaleng.2010.03.012.

[68]   I. G. Zaltsman, "STEFAN-BOLTZMANN LAW," in *A-to-Z Guide to Thermodynamics, Heat and Mass Transfer, and Fluids Engineering*, 2011.

[69]   Magnetorquers, "CubeTorquer and CubeCoil for CubeSat applications," *CubeSatShop*. http://www.cubesatshop.com/wp-content/uploads/2016/06/CubeTorquer-CubeCoil-Brochure-August-2016.pdf (accessed Jun. 05, 2020).

[70]   P110, "High effeciency solar panels," *CubeSatShop*. https://gomspace.com/UserFiles/Subsystems/datasheet/gs-ds-nanopower-p110-210.pdf (accessed Jun. 04, 2020).

[71]   NCTR-M012, "NCTR-M012 Magnetorquer Rod," *CubeSatShop*. https://www.cubesatshop.com/wp-content/uploads/2016/06/NewSpace-Magnetorquer-Rod_7b.pdf. (accessed Jun. 04, 2020).